

Chapter 3

Introduction to LIGO

In this chapter we describe the history of GW detectors and the design of the LIGO GW detectors, which have been built for the detection of GWs. This description is broken up into several parts: a brief history of GW detectors is given in section 3.1, the design of the detectors is described in section 3.2, the dominant noise sources for LIGO are described in section 3.3, the calibration of LIGO is described in section 3.4, the response of the detectors to GWs is given in section 3.5, a description of using multiple detectors in a global network is given in section 3.6, and a description of previous LIGO science runs are given in section 3.7.

3.1 History of Gravitational-Wave Detectors

There exists a rich, and somewhat controversial, history of searching for GWs [49]. In the late 1950s and early 1960s, Weber designed and built the first GW detector in the form of a large, suspended, metal bar [50]. This bar was fit with piezoelectric transducers around its center to measure the oscillations of this driven harmonic oscillator. This bar was isolated from the surrounding environment using a combination of seismic isolation suspensions and a vacuum chamber. As GWs passed through this bar, the dynamical Riemann tensor would induce oscillations of the bar's fundamental mode, giving it the name of a resonant mass detector. These oscillations would then be detected by the transducers and, looking at the fundamental mode oscillations using a Fourier Transform, recorded. Weber's group went on to build several additional detectors so that they could look for coincident triggers (i.e., times when the detectors exhibited excess noise at their resonance frequency).

Results from these searches can be found in Refs. [51, 52] where they find rates of coincident triggers well above the background.

After Weber built this detector and reported data from it, several groups around the world built their own detectors. These group (with detectors located in e.g., Argonne, Glasgow, Moscow, ISR, IBM, Reading, Rutherford, Tokyo, Munich, Frascati, Stanford, Bell Labs, and Rochester [53]) then went on to publish additional papers about the rate of coincident triggers not being consistent with Weber's observations.

The next set of advanced detectors were the ultralow temperature bars Allegro [54], AURIGA [55], Explorer [56], NAUTILUS [57], and Niobe [58]. These detectors further suppressed the noise in the detectors by reducing the temperature of the detectors to a few Kelvin using refrigeration, allowing detector noise temperatures of a few to submilliKelvin levels to be reached. Searches for GWs with these detectors also could not measure a rate above their background.

Another design for resonant mass detectors, a spherical mass rather than a cylindrical bar, was conceived by Forward in Ref. [59]. If we look at the antenna response of the different resonant mass detectors, we see that the bars are sensitive to strains parallel to their cylindrical axis with the response tensor

$$R^{ab} = u_X^a u_X^b, \quad (3.1)$$

where u_X^a is the unit vector along the cylindrical axis of the bar. This implies that these detectors will be relatively insensitive to GWs traveling along this axis as GWs are transverse(-traceless) (TT) waves (see chapter 2).

However, this is not the case for spherical resonant detectors. For spherical detectors, the response tensor would be dependent on the number and locations of transducers, with their locations not being limited to the locations conducive to measuring the fundamental mode. Since GWs are TTwaves, a basis of five tensors is all that is needed in order to determine all directions, polarizations, and

magnitudes of incident GWs [59]. One independent set given by Forward is

$$A^{ab} = \frac{1}{\sqrt{2}}(u_X^a u_X^b - u_Y^a u_Y^b), \quad (3.2a)$$

$$B^{ab} = \frac{1}{\sqrt{6}}(-u_X^a u_X^b - u_Y^a u_Y^b + u_Z^a u_Z^b), \quad (3.2b)$$

$$C^{ab} = \frac{1}{\sqrt{2}}(u_X^a u_Y^b + u_Y^a u_X^b), \quad (3.2c)$$

$$D^{ab} = \frac{1}{\sqrt{2}}(u_X^a u_Z^b + u_Z^a u_X^b), \quad (3.2d)$$

$$E^{ab} = \frac{1}{\sqrt{2}}(u_Y^a u_Z^b + u_Z^a u_Y^b). \quad (3.2e)$$

Several detectors of this sort are being pursued around the world. These include the MiniGRAIL project [60] in Leiden University, the Netherlands and the ‘‘Mario Schenberg’’ GW detector [61] in the University of Sao Paulo, Brazil.

A different detector technology that has also been designed and built is the interferometer detector. This type of detector, in its most basic form, consists of a Michelson Interferometer that measures differential length changes along its two arms. The advantage of this type of detector is that, as one is measuring actual length changes instead of the amplitude of oscillations on resonance of a harmonic oscillator, the bandwidth of the detector can be much larger than that of the resonant mass detectors. If the arms are orthogonal and oriented along the X and Y directions respectively, this type of detector has the response tensor

$$R^{ab} = u_X^a u_X^b - u_Y^a u_Y^b. \quad (3.3)$$

A meter size version of this detector was first used for this purpose by Forward in the 1970s [62], of comparable sensitivity to the bar detectors operating at that time. Around the same time, Weiss analyzed the noise sources of such a detector and developed the first ideas of kilometer-scale devices [63]. This inspiration is what has led to the modern day construction of TAMA300 [64], GEO600 [65], Virgo [66], and the three LIGO detectors [67], all kilometer-scale GW detectors.

Resonant mass detectors are typically sensitive to GWs in the frequency range of 10^3 – 10^4 Hz,

and ground-based interferometer detectors are sensitive to GWs in the frequency range of 10^1 – 10^4 Hz. Other techniques are also currently being pursued to detect GWs in different frequency regions. These include space-based interferometers, such as LISA [68] and DECIGO [69], designed to be sensitive to GWs with frequencies between 10^{-3} – 10^{-2} Hz and 10^{-1} – 10^1 Hz respectively, pulsar timing experiments (first described in Refs. [70, 71]) aimed at detecting very low frequency GWs in the range of 10^{-9} – 10^{-7} Hz, and Cosmic Microwave Background polarization measurements [72, 73, 74, 75, 76, 77, 78, 79, 80, 81] designed to detect GWs in the extremely-low frequency band of 10^{-18} – 10^{-15} Hz.

3.2 Design of LIGO

The LIGO detectors were designed to detect differential strains from incident GWs, based on a simple Michelson Interferometer (see figure 3.1). This design starts with an input laser incident on a beam splitter located at the origin with the face at a 45° angle between the x - and y -axes. The beam splitter directs 50% of the light in two perpendicular directions, x and y . The light travels toward mirrors located at the end of the arms, $(L_x, 0)$ and $(0, L_y)$, which redirect the light back toward the beam splitter. The phase the light accumulates as it travels from the beam splitter to the end mirror is given by

$$\phi = \int_0^L \frac{2\pi}{\lambda} dx = \frac{2\pi L}{\lambda}, \quad (3.4)$$

where L is the distance traveled and λ is the wavelength of the light. The total phase of one round trip will then be the sum of the integral down and the integral back.

When the light returns to the beam splitter, the two beams interfere with each other in such a way that, depending on the differential arm length, the light is either directed back toward the laser (the symmetric port), or toward a photodetector (the antisymmetric port), or some combination of the two. The differential arm length $L_x - L_y$ can then be measured, modulo one wavelength, by

looking at the power of the light coming from the antisymmetric port, P_{AS} . This is given by

$$\begin{aligned} P_{\text{AS}} &= P_0 \sin^2(\phi_x - \phi_y) \\ &= P_0 \sin^2\left(\frac{4\pi}{\lambda}(L_x - L_y)\right), \end{aligned} \quad (3.5)$$

where P_0 is the input laser power, ϕ_x is the phase accumulated for the beam in the x -arm, and ϕ_y is the phase accumulated for the beam in the y -arm. This shows that P_{AS} is dependent on the differential arm length.

Let us assume that the arms are of the same length L , and an incident GW with amplitude h is stretching the detector along the x -axis and squeezing it along the y -axis. We see from chapter 2 that this effect causes the distance the light needs to travel to be given by $L' \approx L(1 \pm h/2)$, giving ϕ_x and ϕ_y as

$$\begin{aligned} \phi_x &= \int_0^{L'} \frac{2\pi}{\lambda} dx - \int_{L'}^0 \frac{2\pi}{\lambda} dx \\ &\approx \frac{4\pi L}{\lambda} \left(1 + \frac{h}{2}\right), \end{aligned} \quad (3.6a)$$

$$\phi_y \approx \frac{4\pi L}{\lambda} \left(1 - \frac{h}{2}\right). \quad (3.6b)$$

With these phase shifts, we find that P_{AS} is then given by

$$P_{\text{AS}} = P_0 \sin\left(4\pi \frac{hL}{\lambda}\right)^2, \quad (3.7)$$

such that for the same change in P_{AS} , the strain h is inversely proportional the length L of the arms. However, although there is a signal at the antisymmetric port for this interferometer, this is a poor way to detect GWs. For one, since the above power at the antisymmetric port is proportional to $\sin^2(\Delta\phi)$, which can be Taylor expanded about zero as $\Delta\phi^2$, the signal we are measuring is *quadratically* proportional to the small GW signal we are trying to sense. In addition, there is no information on which direction we need to move the mirrors to bring the signal back to the dark

fringe.

In order to get around these problems, LIGO has adopted the use of the “heterodyne detection” technique, which combines a phase-modulated input laser with a Schnupp Asymmetry. In this setup, before the laser light enters the interferometer, the light is phase modulated with a frequency Ω such that instead of all the light entering the detector with one frequency, there are effectively three superposed laser beams entering with three different frequencies and electric field amplitudes: the original beam with frequency ω and amplitude E_0 , also known as the *carrier*, and two *sidebands* with frequency $\omega \pm \Omega$ and amplitude E_1 .

When the arm lengths are perfectly equal, all of these beams will come out at the symmetric port, which results in the same answer as above. However, there is a different response when a Schnupp Asymmetry is introduced between the arms. This occurs when the arms of the interferometer are *unequal* by an amount that is an integer number of wavelengths of the carrier light but *not* an integer of wavelengths for the sidebands. In this situation, in the absence of a GW signal, the carrier light will come out the symmetric port while the sidebands will be transmitted to the antisymmetric port. When there is a GW signal present, a phase shift will be introduced on all three beams such that a mixture of all three beams will exit the antisymmetric port. Processing the signal coming from the antisymmetric port with demodulation results in an error signal that is *linear* in the GW amplitude, just as is needed.

In order to increase the sensitivity of the detector, LIGO uses two modifications to the standard Michelson interferometer. The first is the use of Fabry-Perot cavities in the two arms in order to increase the storage time of light within the arms, effectively increasing the length of the arms, and thus the phase shift on the light, by the same factor. The second is to boost the light circulating within the interferometer for a given laser input power with the addition of a power-recycling mirror. A schematic for the design of LIGO, including all of the additions to the standard Michelson interferometer, can be seen in figure 3.1.

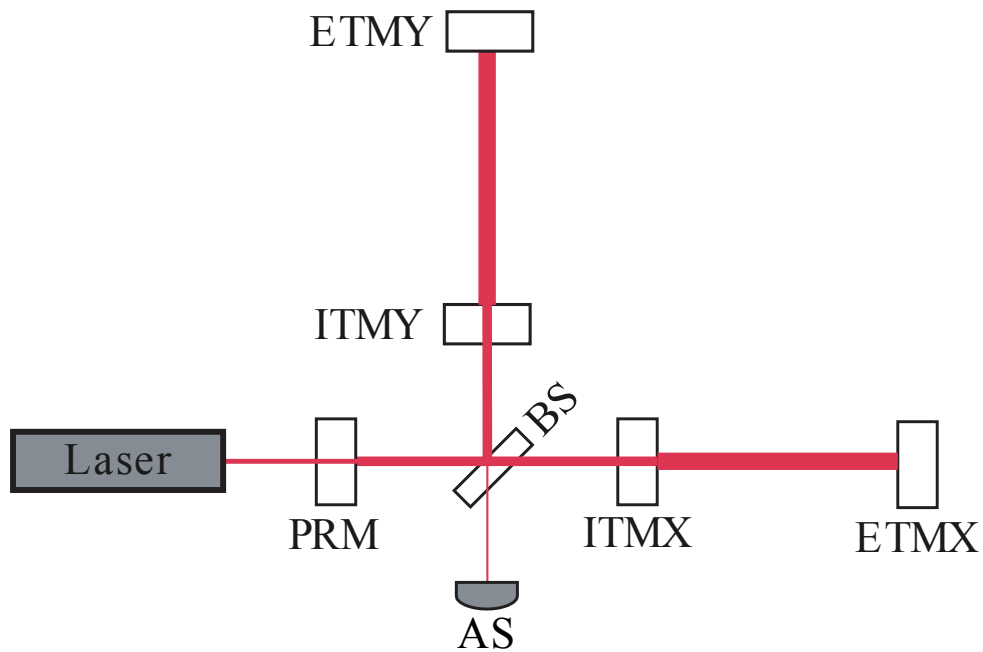


Figure 3.1: LIGO Schematic

A simple schematic of the LIGO detectors. The mirror labels are as follows: PRM (power recycling mirror), BS (beam splitter), ITMX/Y (x -/ y - arm input test mass), ETMX/Y (x -/ y - arm end test mass), AS (antisymmetric port). The width of the laser beam denotes power in different portions of the detector. A simple Michelson interferometer includes the mirrors BS and ETMX/Y. The addition of the ITMX/Y mirrors makes use of Fabry-Perot cavities for the arms. The use of the PRM boosts the power circulating in the whole interferometer.

3.3 Dominant Noise Sources

The design sensitivity of the LIGO detectors is limited by several fundamental noise sources for different frequency bands [82]: Seismic Noise for $f < 40$ Hz, suspension thermal noise for $40 \text{ Hz} < f < 150$ Hz, and photon shot noise for $f > 150$ Hz.

Seismic Noise is the result of ground motion coupling to the motion of the mirrors. This type of noise is suppressed in multiple ways, both actively and passively. Passive isolation is achieved by suspending the mirrors as pendula, on seismic isolation stacks. This suspension acts as a low pass filter for motion coming from the ground, resulting in a pendulum response function for the mirror motion that dies as $1/f^2$ for noise above the resonant frequency. Active isolation is also used by sensing ground motion and feeding this back into the controls of the Hydraulic External Pre-Isolator for cancellation.

Suspension Thermal Noise results from the random thermal motions of the room-temperature suspension feeding into motions of the mirrors. This motion has been calculated by Saulson in Ref. [83].

Photon Shot Noise results from a finite number of photons arriving each second, informing us of the motion of the mirrors. Since we are limited in the number of photons that arrive at the photodetector per second by the power of the laser light, we end up not being able to detect strains better than [82]

$$\Delta h[\text{Hz}]^{-1/2} = \frac{1}{L} \left(\frac{hc\lambda}{\pi^2 P} \right)^{1/2}, \quad (3.8)$$

where h is Planck's constant, c is the speed of light, λ is the wavelength of the laser light, and P is the power of the laser light. The arm cavity introduces an enhancement in P at the expense of reduced sensitivity at high frequencies due to the cavity pole. This results in a shot-noise equivalent strain that rises with f above the cavity pole frequency of ~ 90 Hz.

These are not the only noise sources in the LIGO detectors. figure 3.2 shows all of the known noise sources during the S5 run [84]. There the noise in channel that carries the GW signal (DARM) is compared to the sum of all the known noise sources (Total). Above 100 Hz, the dominant noise

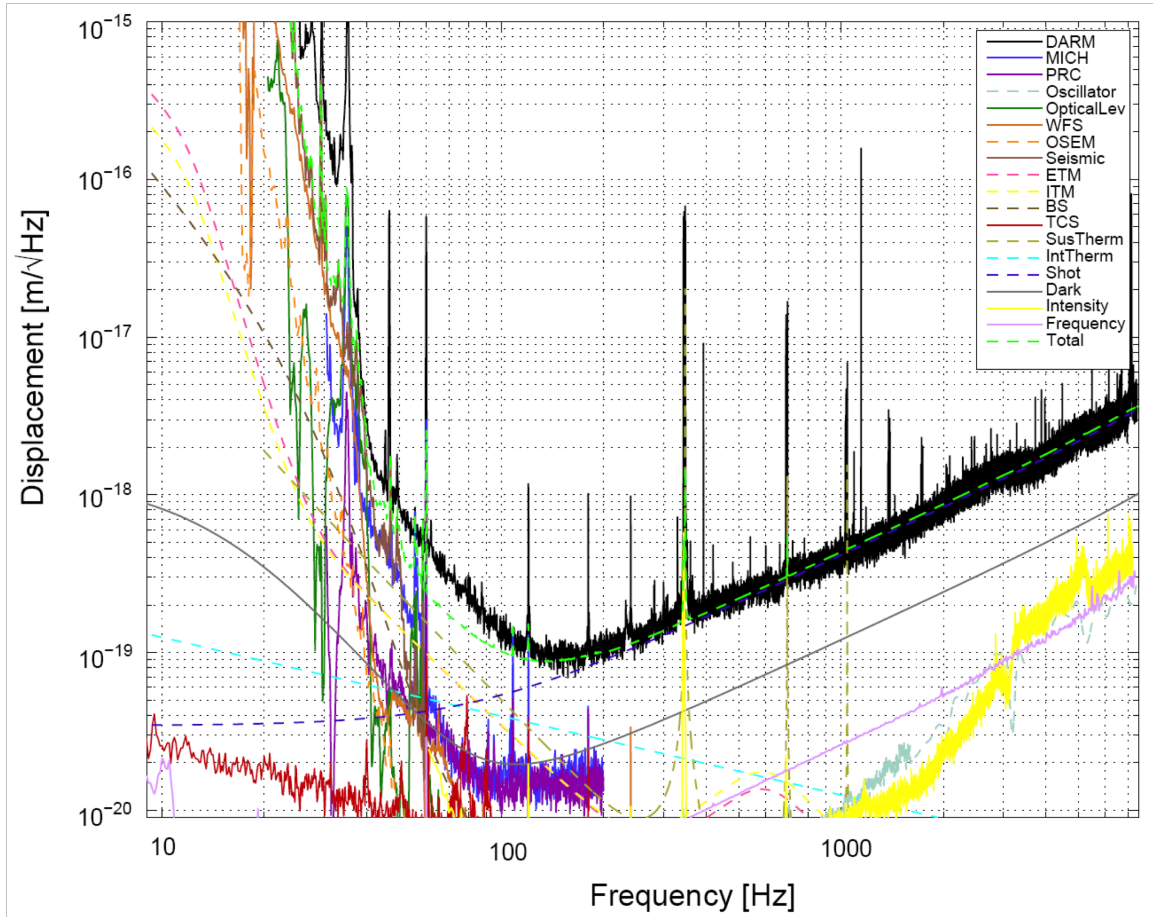


Figure 3.2: LIGO Noise Budget

The noise budget for the 4 km instrument at Hanford from Ref. [84]. The line labeled “Total” is the sum of all known noise sources. The black line (measured DARM noise) should be compared to this.

source is shot noise and DARM agrees very well with Total. Between 50 and 100 Hz there are noise sources that have not been accounted for in addition to the expected dominant source, which is suspension thermal noise. Below 50 Hz the noise is mainly due to man-made activities and is highly nonstationary, thus it is hard to estimate at any given point in time.

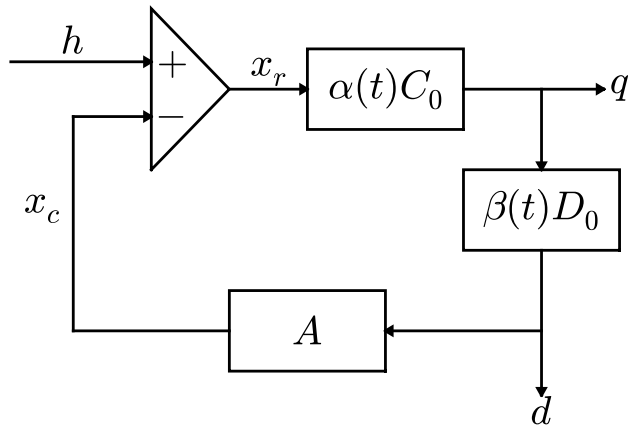


Figure 3.3: Model Control Loop

A simple model for the control loop of the LIGO length sensing and control system [85].

3.4 Calibration

In this setup, the light incident on the antisymmetric port's photodetector carries the information of the strain the detector is experiencing. However, in order to keep the detectors in a stable data-taking mode, this signal is fed back into detector such that the light arriving from the antisymmetric port is kept roughly constant. This means that the strain of the detector must be reconstructed from the signal arriving from the antisymmetric port, known as the error signal q , and the transformations made on q to control the detector, what we call the response function R . This reconstruction is easily understood in the frequency domain as [85]

$$h(f) = R(f)q(f) . \quad (3.9)$$

The feedback loop diagram for this control system is shown in figure 3.3. In the frequency

domain, the relationships depicted in the diagram take the simple form

$$x_r(f) = h(f) + x_c(f), \quad (3.10a)$$

$$q(f) = \alpha(t)C_0(f)x_r(f), \quad (3.10b)$$

$$d(f) = \beta(t)D_0(f)q(f), \quad (3.10c)$$

$$x_c(f) = A(f)d(f), \quad (3.10d)$$

where $C_0(f)$ is a reference sensing function measured at some reference time whose frequency dependence is determined primarily by the Fabry-Perot arm cavities and is roughly $(1 - f/f_p)^{-1}$ with $f_p \approx 90$ Hz and $\alpha(t)$ is a real overall gain that depends on the light power stored in the arms and is measured every ~ 10 seconds, A is an actuation function that is largely determined by the pendulum suspension of the mirrors, and D_0 is the feedback filter and $\beta(t)$ is a real overall gain.

From these relations, $R(f)$ is found to be

$$R(f) = \frac{1 + \alpha(t)\beta(t)G_0(f)}{\alpha(t)C_0(f)}, \quad (3.11)$$

where $G_0(f)$ is the reference open loop gain given by

$$G_0(f) = A(f)C_0(f)D_0(f), \quad (3.12)$$

which has a unity gain frequency of ~ 150 Hz. The time-dependent gain factors $\alpha(t)$ and $\beta(t)$ are measured by tracking the amplitude of calibration lines that are injected into the detectors at around 1 kHz, 150 Hz, and a few tens of Hz.

This procedure tells us how to calibrate the error signal from the detector in order to obtain the strain signal in the frequency domain. However, for LIGO's fifth science run (S5), an additional step was added to the calibration [85], giving the strain signal in the time domain $h(t)$. This is the main method used for analyses of the S5 data.

3.5 Interferometer Antenna Response

In chapter 2, we described the effect of incident GWs on test particles perpendicular to the direction of propagation of the waves. We noted that interferometric detectors have a response tensor, in the reference frame of the beam splitter, of the form

$$R^{\alpha\beta} = \begin{pmatrix} 0 & 0 & 0 & 0 \\ 0 & 1 & 0 & 0 \\ 0 & 0 & -1 & 0 \\ 0 & 0 & 0 & 0 \end{pmatrix}. \quad (3.13)$$

The resulting response of the detector is given by

$$\frac{\Delta l}{l} = \frac{1}{2} h_{\alpha\beta} R^{\alpha\beta}. \quad (3.14)$$

GWs from arbitrary directions will have different projections onto this response tensor. Here we describe those projections as the antenna response of the detector to GWs incident from directions given by θ and ϕ , and the polarization angle ψ , which bring equation (3.14) into the form

$$\frac{\Delta l}{l} = F_+ h_+ + F_\times h_\times, \quad (3.15)$$

where F_+ and F_\times are the antenna factors we are evaluating. The above angles are identified in figure 3.4.

In this derivation we start with the assumption that the wavelength of the GW is much longer than the storage time of the light in the interferometer's arms times the speed of light $\lambda \gg cT$.

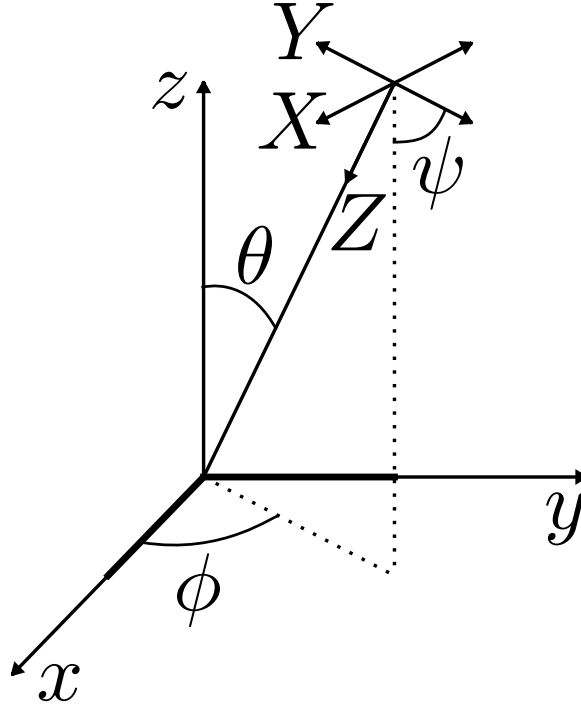


Figure 3.4: Euler Angles

The Euler angles $\{\phi, \theta, \psi\}$ used in converting from the GW propagation frame $\{X, Y, Z\}$ to the detector frame $\{x, y, z\}$.

In the radiation frame, denoted with ${}^{\prime}$ s above the indices, the GW $h_{\alpha'\beta'}$ is given by

$$h_{\alpha'\beta'} = \begin{pmatrix} 0 & 0 & 0 & 0 \\ 0 & h_+ & h_\times & 0 \\ 0 & h_\times & h_+ & 0 \\ 0 & 0 & 0 & 0 \end{pmatrix}, \quad (3.16)$$

which can be split into

$$h_{\alpha'\beta'} = S_{\alpha'\beta'}^+ h_+ + S_{\alpha'\beta'}^\times h_\times. \quad (3.17)$$

To transform this into frame of the detector (i.e., the frame of the beam splitter) we need to transform both indices of $h_{\alpha'\beta'}$. This transformation can be seen as the combination of different

Euler angle rotations with the combined rotation matrix given by

$$\begin{aligned}
R_{\alpha}^{\alpha'} &= \begin{pmatrix} 0 & 0 & 0 & 0 \\ 0 & -\cos \theta \cos \phi \cos \psi - \sin \phi \sin \psi & -\cos \theta \cos \phi \sin \psi + \sin \phi \cos \psi & \sin \theta \cos \phi \\ 0 & \cos \theta \sin \phi \cos \psi - \cos \phi \sin \psi & \cos \theta \sin \phi \sin \psi + \cos \phi \cos \psi & -\sin \theta \sin \phi \\ 0 & -\sin \theta \cos \psi & -\sin \theta \sin \psi & -\cos \theta \end{pmatrix} \\
&= \begin{pmatrix} 0 & 0 & 0 & 0 \\ 0 & A & B & C \\ 0 & D & E & F \\ 0 & G & H & I \end{pmatrix}. \tag{3.18}
\end{aligned}$$

Applying this to B_+ and B_{\times} , we find

$$S_{\alpha\beta}^+ = \begin{pmatrix} 0 & 0 & 0 & 0 \\ 0 & A^2 - D^2 & AB - DE & AC - DF \\ 0 & AB - DE & B^2 - E^2 & BC - EF \\ 0 & AC - DF & BC - EF & C^2 - F^2 \end{pmatrix}, \tag{3.19a}$$

$$S_{\alpha\beta}^{\times} = \begin{pmatrix} 0 & 0 & 0 & 0 \\ 0 & 2AD & AE + BD & AF + CD \\ 0 & BD + AE & 2EB & BF + CE \\ 0 & CD + AF & CE + BF & 2CF \end{pmatrix}. \tag{3.19b}$$

We can now calculate the antenna factors where $F_+ = (1/2)S_{\alpha\beta}^+ R^{\alpha\beta}$ and $F_{\times} = (1/2)S_{\alpha\beta}^{\times} R^{\alpha\beta}$ resulting in

$$F_+ = \frac{1}{2} (1 + \cos^2 \theta) \cos 2\phi \cos 2\psi + \cos \theta \sin 2\phi \sin 2\psi, \tag{3.20a}$$

$$F_{\times} = \frac{1}{2} (1 + \cos^2 \theta) \cos 2\phi \sin 2\psi + \cos \theta \sin 2\phi \cos 2\psi. \tag{3.20b}$$

We can see the structure of these antenna factors when plotted with $\psi = 0$ in figure 3.5. From

these we find that there are several regions of the sky where the detectors are sensitive to neither polarization, which we call nodes.

There is one additional angle that will affect the amplitude of the signal that a interferometer detector will receive from a quasi-circular inspiralling compact binary, the angle of inclination ι between the orbital plane and vector connecting the origin of the detector and the origin of the source. This will have an effect on resulting signal seen by the detector $h(t)$ such that

$$h(t) = h_+(t)F_+(1 + \cos^2 \iota) + h_\times(t)F_\times(2 \cos \iota) . \quad (3.21)$$

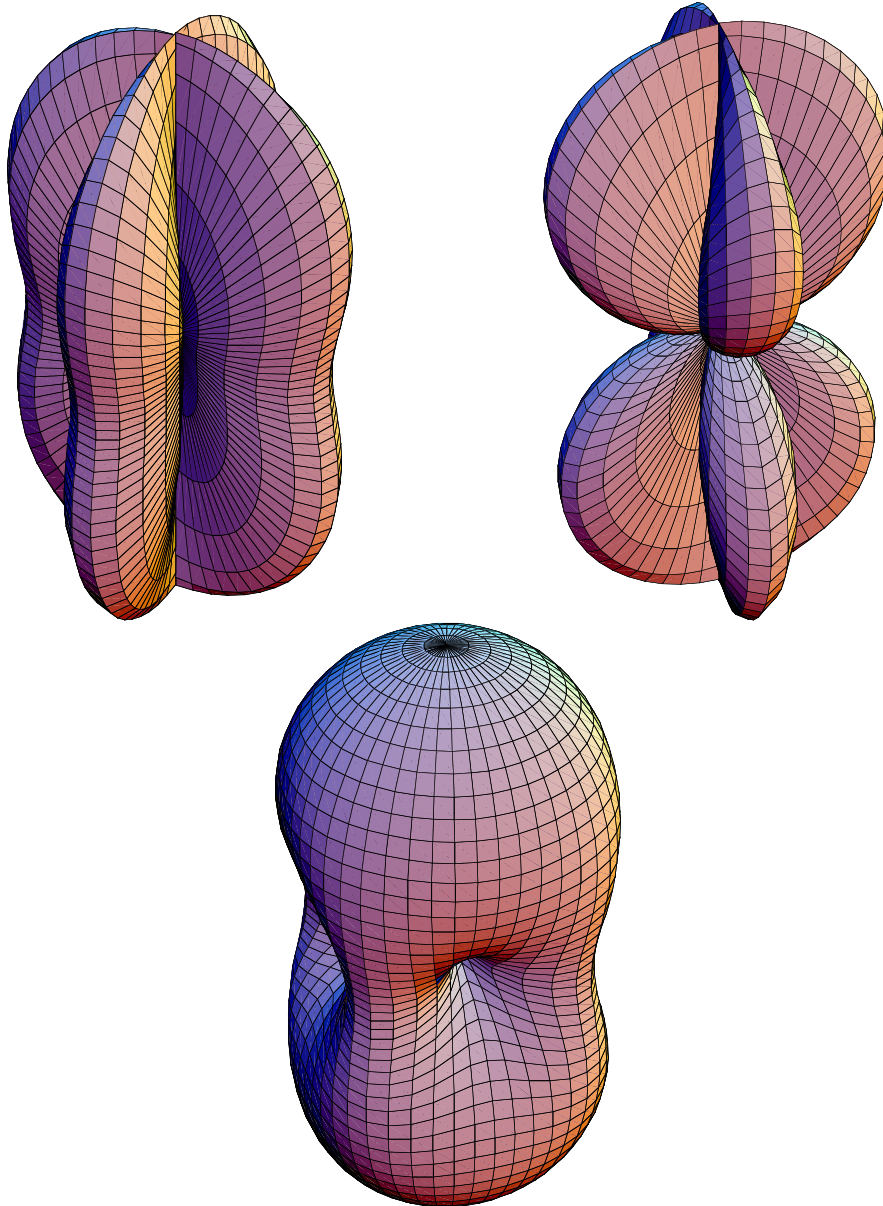


Figure 3.5: Detector Antenna Patterns

The antenna patterns for interferometer detectors for plus (top left), cross (top right), and combined (bottom) polarizations with polarization angle $\psi = 0$. For this figure, the detectors arms are oriented such that the first node in the bottom plot is found at 45° between the two arms of the detector and subsequent nodes occur every 90° as you rotate around the vertical axis.

Table 3.1: Combined Horizon Volumes

Detector Combination	Volume (Mpc ³)
H1H2	2.13×10^3
H2L1	2.11×10^3
H2V1	1.81×10^3
H2L1V1	8.84×10^3
H1L1	1.23×10^4
H1H2L1	
H1V1	8.68×10^3
H1H2V1	
H1L1V1	1.54×10^4
H1H2L1V1	

The combined horizon volume to which each detector combination is sensitive. When calculating this, we compute the distance at which each detector would see a binary neutron star signal with inclination angle ι at an SNR of 8. For each point in the sky and each polarization ψ , we take the distance from the second most sensitive detector (i.e. only double coincident observations are required), volume-averaged over ψ and ι , and then integrate over the sky. These calculations are done using the design sensitivity of each detector.

3.6 Networks of Detectors

As was discussed above, coincidence can be used to verify a GW signal when it is seen by multiple detectors. However, this can only be done when at least two detectors see a signal. One common way to quantify the sensitivity of a detector is by looking at the distance at which a given detector can see a optimally located and oriented binary neutron star signal (i.e., an overhead, face on orbit; $\theta = \phi = \psi = \iota = 0$) with an SNR of 8. This is referred to as the horizon distance. Non-optimally located and oriented sources can be detected with SNR = 8 at shorter distances. Table 3.1 shows the volumes of space that are screened after averaging over all of these angles when different combinations of interferometric GW detectors are operating. The angle-averaged sky maps associated with each detector and combination of detectors can be seen in figure 3.6 and 3.7 respectively, which are Mollweide projections of the sky. As additional detectors are built around the world, we will be able to more completely cover the sky.

Just as combining the signals from different transducers on a spherical resonant mass detector allows us to determine the sky location and polarization of a given signal, coherently combining the output from multiple, misaligned interferometric detectors accomplishes the same thing [86]. Another advantage of coherent combinations of signals is the amplification of the signal relative to

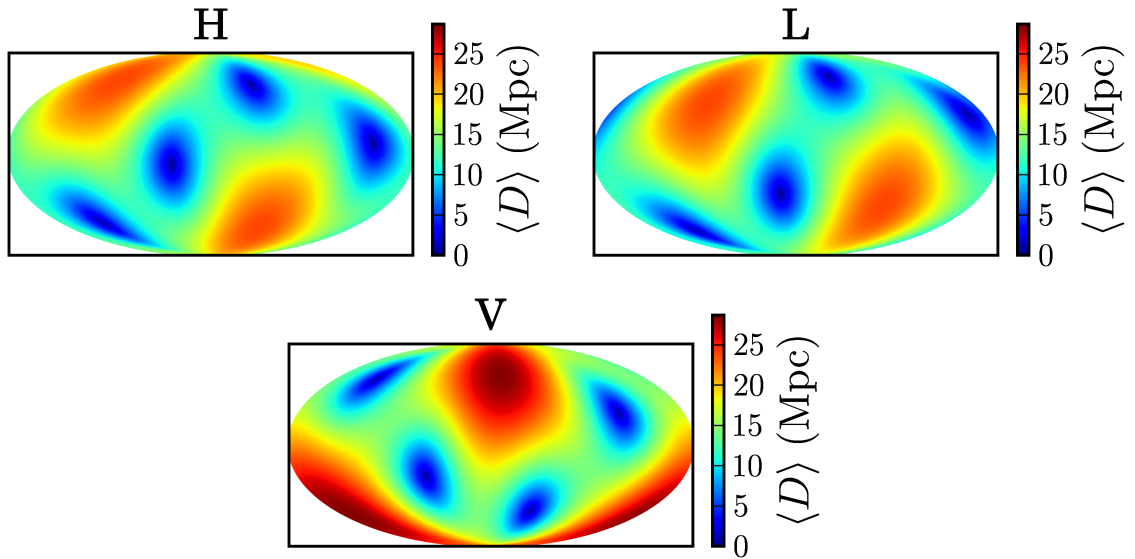


Figure 3.6: Individual Detector Angle-Average Sky Maps

The Hanford (top left), Livingston (top right), and Virgo (bottom) angle-averaged sky maps for their design sensitivities. The color scale shows the average distance at which each detector can see a binary neutron star signal with an SNR of 8, volume-averaged over the polarization and inclination angles.

the noise in the detectors. Because the noise in the different detectors is independent random noise, when the signals are combined, the random fluctuations are suppressed through incoherent addition while external GW signals add coherently.

A final advantage of coherent analysis is the overdetermination of the signal from multiple data streams. When at least three detectors are used, since there are only two independent polarizations of a GW signal, the data from the detectors can be combined in such a way that the signal should be cancelled out. This type of combination, called a null-combination, can be used to identify an accidental coincidence of noise triggers in the detector network since this will cause excess energy in all the detectors that is incoherent.

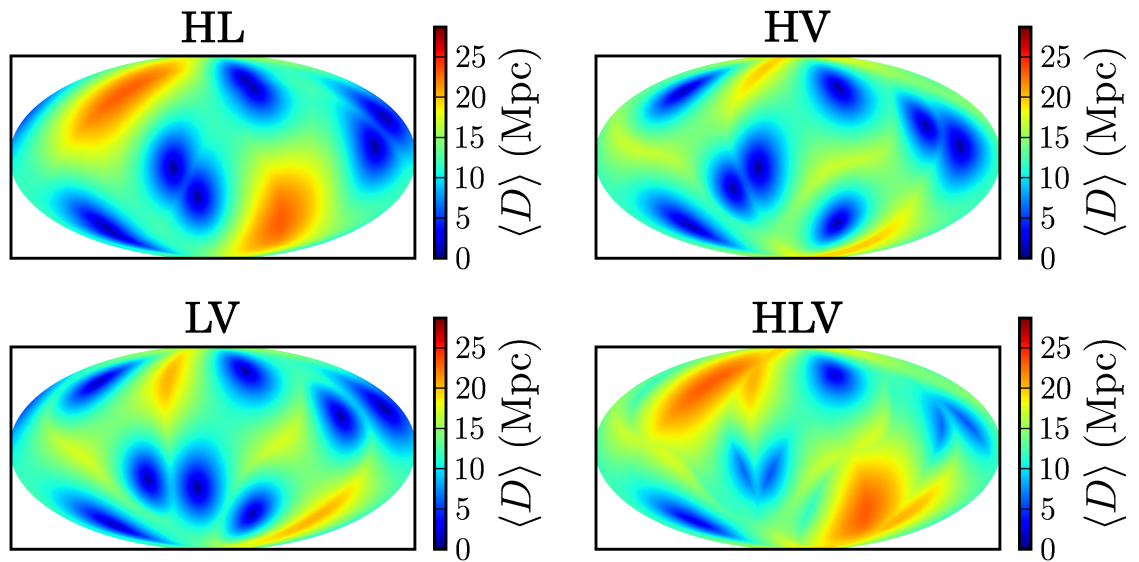


Figure 3.7: Combined Detector Angle-Average Sky Maps
 The Hanford-Livingston (top left), Hanford-Virgo (top right), Livingston-Virgo (bottom left), and Hanford-Livingston-Virgo (bottom right) combined angle-averaged sky maps for their design sensitivities. The color scale shows the average distance at which each that detector combination can see a binary neutron star signal with an SNR of 8, volume-averaged over the polarization and inclination angles.

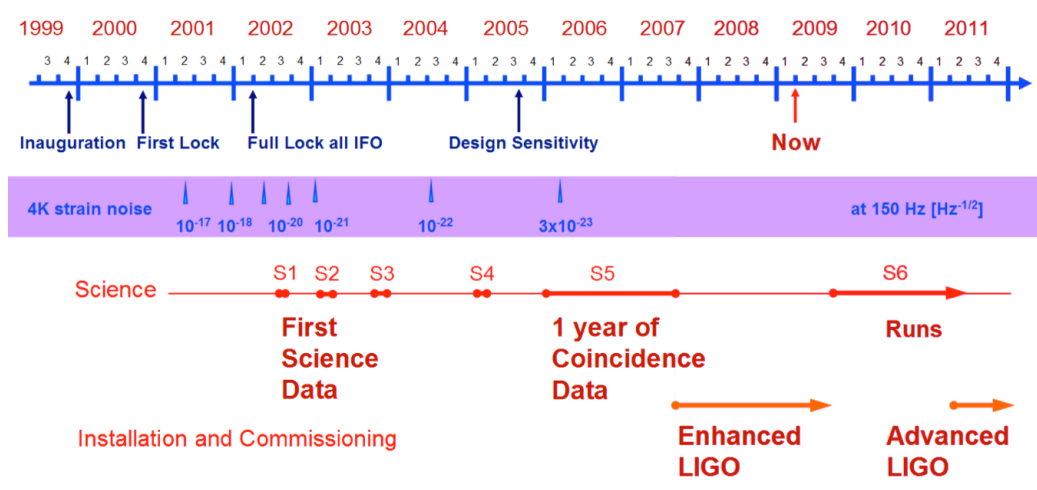


Figure 3.8: LIGO Science Runs Timeline

A timeline showing the progress made in the LIGO detectors strain sensitivity as well as the different periods of science data taking [84].

3.7 LIGO's Past and Future

After the LIGO detectors were built, there were several times when science data was taken in between commissioning periods on their way toward their design sensitivity (figure 3.8). These science runs (S1–S4) were analyzed for many different types of signals [17, 18, 19, 20, 21, 22, 23, 24, 25, 26, 27, 28, 29, 30, 31, 32, 33, 34, 35, 36, 37, 38, 39, 40, 41, 42, 43, 44, 45, 46, 47, 48]. One of the important aspects of these runs was finding times during which the detectors were not operating properly. During these times, many auxiliary channels of the detectors were recorded and analyzed, leading to the discovery of different ways the interferometers glitch and the suppression of such glitches during the next commissioning break.

In the upcoming months, the LIGO detectors will finish being upgraded from their initial design (Initial LIGO) to their enhanced design (called enhanced LIGO) and will start taking data for their sixth science run with an expected factor of two increase in sensitivity over S5. A few years later, the detectors will be taken offline again to undergo a more extensive reworking, returning with their advanced design (Advanced LIGO) in place, which should further improve the sensitivity by an order of magnitude with respect to Initial LIGO.